Synthesis, Characterization, and Studies on Photophysical Properties of Rhodamine Derivatives and Metal Complexes in Dye-Sensitized Solar Cells

Oyedoyin Aduroja, MdRafsun Jani, William Ghann, Saquib Ahmed, Jamal Uddin,* and Fasil Abebe*

Read Online

ACCESS | Metrics & More | Article Recommendations | SI Supporting Information

ABSTRACT: Rhodamine 6G dyes are low-cost, highly soluble fluorescent dyes frequently utilized as laser dyes, chemical sensors, and as tracer dyes in the determination of the direction and rate of flow of water. In this study, the photophysical properties of three rhodamine 6G dyes, bearing phenyl (**P15**), furan (**P41**), and 5-hydroxymethyl furan (**P45**), and their metal complexes were investigated using ultraviolet−visible (UV−vis) spectroscopy, fluorescence spectroscopy, fluorescence lifetime, and Fourier transform infrared (FTIR) measurements. Rhodamine 6G dyes and their complexes were subsequently applied as sensitizing dyes in the fabrication of dye-sensitized solar cells, and the solar to electric power efficiency and electrochemical impedance spectros-
copy measurements were performed. The solar to electric power efficiency values of the metal complexes of the rhodamine 6G dyes were higher than those of the devices fabricated with only rhodamine dyes without copper (II). The most significant change was observed in rhodamine P41 with a 30% increase in solar to electric power efficiency when the dye was conjugated to the copper ion.
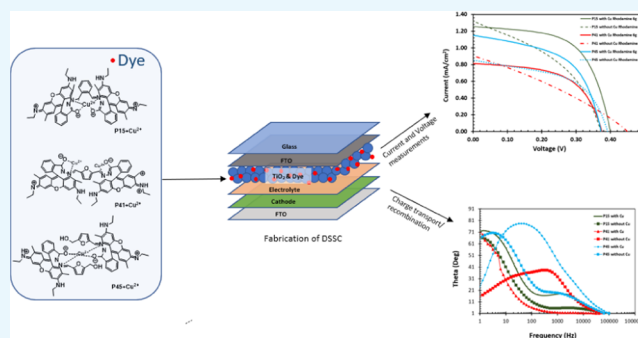
1. INTRODUCTION

Dye-sensitized solar cells (DSSC) convert solar power to electrical power using a photosensitizing dye that is responsible for harnessing the solar energy.[1−3] The process for the generation of electricity in dye-sensitized solar cells comprises three main steps, which include the harnessing of solar energy, separation of charge, and catalytic reactions. DSSCs are popular and are the subject of several scientific research studies due to the facts that they are low-cost, materials for their production are readily available, and they are environmentally friendly. Different types of dye have been utilized in the fabrication of dye-sensitized solar cells with varying percen-tages of solar power-to-electric power efficiencies. These dyes include ruthenium-based dyes,[4−10] prophyrins,[11−14] cya-nines,[15−17] natural dyes,[18−21] and other synthetic dyes.[22−24] Rhodamine dyes are fluorescent dyes, which are soluble in many solvents and could be used in the fabrication of dye-sensitized solar cells.[25]

Rhodamine dyes are fluorescent compounds with superior brightness, outstanding photostability, and high fluorescence quantum yield, and their properties could be altered through substitution. The excellent properties of rhodamine dyes have made them versatile for use in immunodiagnostics, fluo-rescence spectroscopy, whole-body imaging, and microarray analysis.[26]

Copper is a significant metal in biological, environmental, and chemical systems. It is the third most abundant metal in

human bodies among essential heavy metals. An essential goal for chemists is to develop a rapid, sensitive, and practical chemosensor for the detection of heavy and transition metal ions.[27] Copper ion (Cu^{2+}) is a major metal pollutant due to its extensive use in the biological and chemical industries. In this study, the effect of copper on the photophysical properties of three rhodamine dyes are investigated. Also, the impact of copper on the performance of rhodamine dye-sensitized solar cells is evaluated.

The experimentally generated data were verified with a theoretical study via SCAPS-1D software. The presence of oxygen vacancies (V_O) in TiO_2 nanostructures changes their electrical and optical characteristics. With increased V_O concentrations, TiO_2 loses its crystallinity and develops more amorphous properties.[28−30] A mixed state of Ti^{4+} and Ti^{3+} is created by oxygen vacancies, and transition of Ti^{4+} to Ti^{3+} accelerates as the defect density of V_O increases.[31] Through X-ray absorption spectroscopy, photoemission spectroscopy, and scanning tunneling spectroscopy, the oxygen vacancy is found on the surface level of TiO_2 nanostructures.[32−34] With an

Scheme 1. Microwave-Assisted Synthesis of P15, P41, and P45
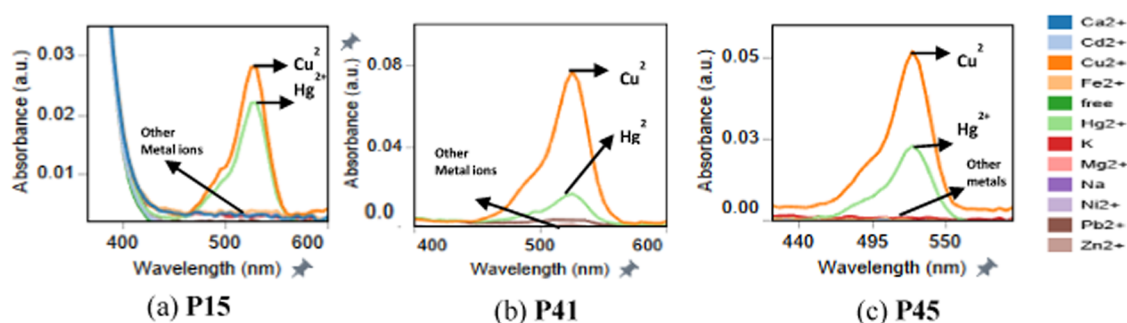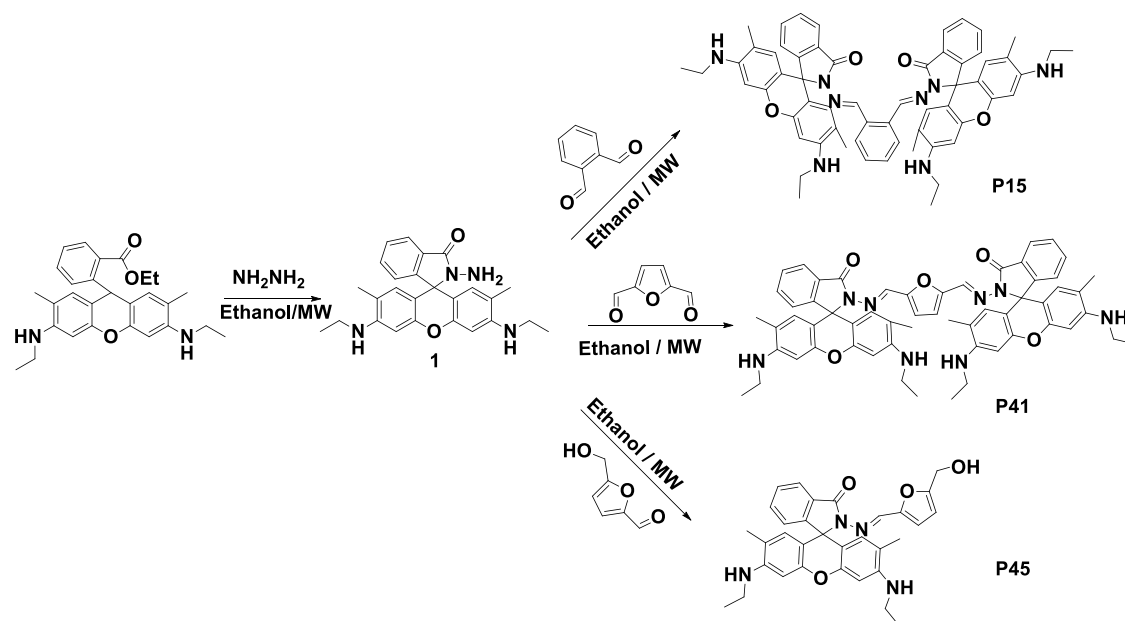
Figure 1. UV−vis spectra of 20 μM (a) **P15**, (b) **P41**, and (c) **P45** with 20 mM metal ions in CH_3CN/H_2O (7:3 v/v) solution.

applied electric field, the subsurface-level oxygen vacancy can be stabilized in the surface level. The subsurface-level oxygen vacancy has an energy level of above 2.2 eV from the valance band maximum (VBM) of TiO2.[35−37] This deep defect state is ascribed to polarons produced by V_O. The Ti atoms get relaxed around the V_O by reducing the Ti−O bond length.[38] Furthermore, shallow level defects are also created by the subsurface-level V_O, hydroxyl group, and Ti interstitial (Tii).[28,38−42] These shallow defects can be situated 0.1−0.2 eV below the conduction band minimum (CBM) of TiO_2 and make the Fermi level close to the CBM.[43] However, the theoretical interpretation of the coexistence of shallow and deep defect states has not been properly explained.

Thus, in this paper, we have utilized the SCAPS-1D software tool to simulate the photovoltaic outputs of the six DSSCs of different dyes and predicted the types of defects presented in the devices and their characteristics.

Scheme 1 shows the structure of the rhodamine 6G dyes utilized in the study. Like all rhodamine compounds, these dyes possess an oxygen atom in a central six-member ring and thus belong to the xanthene class of dyes. Each of the rhodamine 6G compounds possess the rhodamine dye and differ in the kind of linkers used to modify it. **P41** and **P45** have the furan ring and only differ in the hydroxyl methylene group located on **P45**. The **P15** on the other hand has the

phenyl ring. The hydroxyl group on **P45** is very important as it enhances the interaction of the dye with the titanium dioxide.

2. RESULTS AND DISCUSSION

In this study, we synthesized rhodamine 6G-based dye sensors following published methods. **P15 and P41** undergo Schiff-base condensation in 1:2 ratio, while only **P45** undergo Schiff-base condensation in 1:1 ratio. All reactions took place with ethanol as a solvent. Highly purified products with good yields have been collected from the solution. The structures of the intermediate and the final products are confirmed by ^{1}H NMR, ^{13}C NMR, and high-resolution mass spectrometry (HRMS) (Figures S1−S9).

2.1. Absorption Spectral Studies. The photophysical study of the rhodamine 6G dyes, bearing phenyl (**P15**), furan (**P41**), and 5-hydroxymethyl furan (**P45**), and their metal complexes was conducted to understand the effect of the metal complex on the photophysical properties on the rhodamine and their application in dye-sensitized solar cells. The UV−vis absorption behaviors of the sensors **P15, P41, and P45** were investigated with the addition of a 20 equiv excess of other metal ions such as Na^+, K^+, Mg^{2+}, Ca^{2+}, Ni^{2+}, Zn^{2+}, Co^{2+}, Hg^{2+}, Pb^{2+}, Fe^{2+}, Fe^{3+}, Cd^{2+}, and Cu^{2+} in aqueous acetonitrile Tris−HCl buffer (10 mM, pH 7.2). Free compounds show no significant absorption peak in the visible range due to the
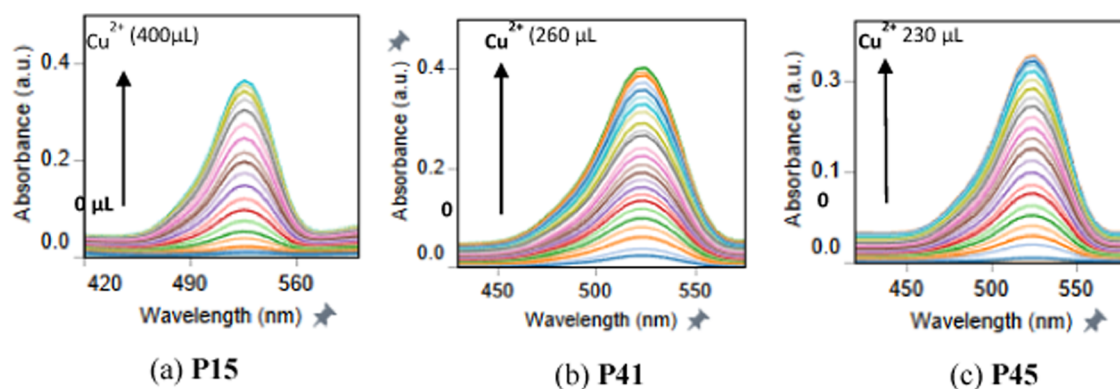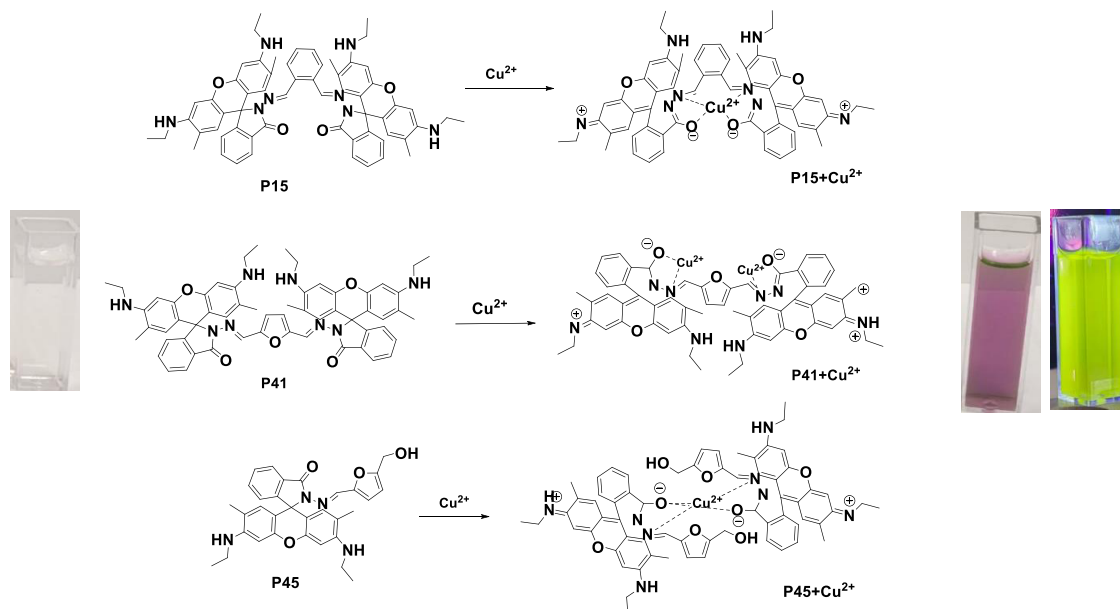
Figure 2. UV−vis spectra of 20 μM (a) **P15**, (b) **P41**, and (c) **P45** with incremental addition of Cu^{2+} in CH_3CN/H_2O (7:3 v/v) solution.

Scheme 2. Proposed Binding Mechanism of the Chemosensors P15, P41, and P45

presence of a closed spirolactam ring (Figure 1). Upon addition of Cu^{2+}, a new absorption band appears at 530 nm, which was attributed to the ring opening reaction of the rhodamine core, while almost no significant enhancement is observed in the presence of other metal ions. The three compounds show an absorption peak for Hg^{2+}, but there was no color change. These sensors showed color change from colorless to a significant pink color toward Cu^{2+} ions. Therefore, it was indicated that compounds **P15**, **P41, and P45** could differentiate Cu^{2+} from other metal ions. The solution changed pink instantaneously with increasing intensity upon the addition of Cu^{2+} concentration as shown in (Figure 2), which can be attributed to the formation of the ring-opened amide followed by the formation of a complex between **P15**, **P41**, and **P45** with the Cu^{2+} ion (Scheme 2). The color of the solution changes from colorless to pink, allowing "naked-eye" detection of Cu^{2+}. The increment in absorbance at 530 nm gets saturated with the addition of 5 equiv of the Cu^{2+} ion.

2.2. Binding Mode and Reaction Mechanism. Subsequently, we investigated the binding stoichiometry between dye sensors **P15**, **P41**, and **P45** and Cu^{2+} using Job's method 27,. Various molar ratios between each dye sensor and Cu^{2+} metal ions were measured. As shown in (Figure 3), the maximum point for **P41** and **P45** appeared at a mole fraction
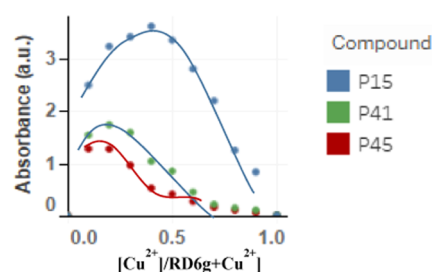

Figure 3. Job's plot for determination of each compound (**P15**, **P41**, and **P45**)−Cu^{2+} complex (50 mM) in CH_3CN/H_2O (7:3 v/v) solution.

of 0.3, while **P15** showed a mole fraction of 0.5; the results proved that the sensors **P41** and **P45** formed a 1:2 copper (II) complex, whereas **P15** forms a 1:1 complex with Cu^{2+}.

2.3. Fluorescence Emission Study. The fluorescence spectra of **P15**, **P41**, and **P45** were characterized simultaneously with the UV spectral analysis in the presence of cations. The emission spectra displayed a similar behavior as UV−vis absorption spectra. The excitation wavelength used was 500 nm with excitation and emission slits of 5 nm. As shown in Figure 4, the free rhodamine compound displayed a
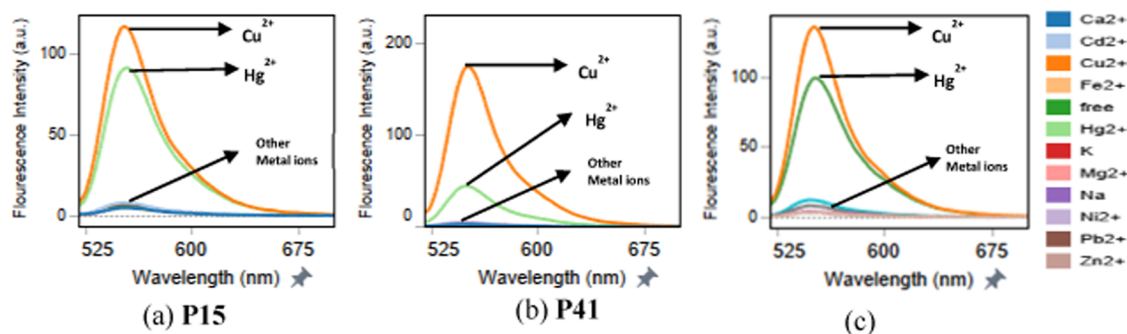
Figure 4. Fluorescence spectra of 20 μM (a) **P15**, (b) **P41**, and (c) **P45** with 20 mM metal ions in CH$_3$CN/H$_2$O (7:3 v/v) solution (λ_{ex} = 500nm).
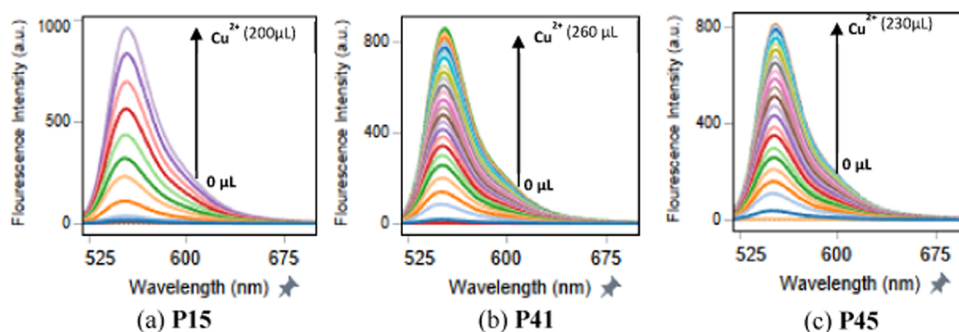

Figure 5. Fluorescence spectral titration of 20 μM (a) **P15**, (b) **P41**, and (c) **P45** with the incremental addition of Cu^{2+} (0−5 equiv) in CH$_3$CN/H$_2$O (7:3 v/v) solution (λ_{ex} = 500 nm).

weak fluorescence emission band and was colorless. However, after adding a variety of metal ions to each rhodamine solution, these sensors did not show any visible fluorescence emission responses to these metal ions except for Cu^{2+} at 565 nm, which indicates that compounds **P15**, **P41**, and **P45** are excellent turn-on sensors for Cu^{2+}. The fluorescence enhancement at 565 nm was attributed to the interaction of Cu^{2+} with sensors, leading to opening of the spirolactam ring of rhodamine compounds **P15**, **P41**, and **P45**. However, no significant variation in the fluorescence spectra was observed with any other metal ion under identical conditions as shown in Figure 5.

The fluorescence lifetime values of the rhodamine dyes and their copper (II) complexes were also investigated as part of the photophysical studies of the dyes. Lifetime measurements were carried out by the method of time-correlated single-photon counting (TCSPC). Analysis of the fluorescence decay curves was carried out by iterative reconvolution fitting with an appropriate prompt or instrument response function (IRF) using a proprietary algorithm implemented in *Horiba DAS6*. For all the samples, it was clear that the incorporation of the metal ion impacted the lifetime of the corresponding complexes. All the dyes and their corresponding complexes exhibited second-exponential characteristics (Figure 6 and Table 1). The rhodamine **P15** had the longest lifetime followed by the rhodamine **P41** and then the rhodamine **P45**. In the case of the rhodamine **P41** and **P45**, there was an increase in the first exponential upon the addition of the metal.

2.4. FTIR Measurements. FTIR of the rhodamine dye-sensitized titanium dye oxide film was carried out to better understand bonds involved in the titanium dioxide and the rhodamine dye. Furthermore, to confirm the mechanism of interaction between the sensors and Cu^{2+}, infrared (IR)
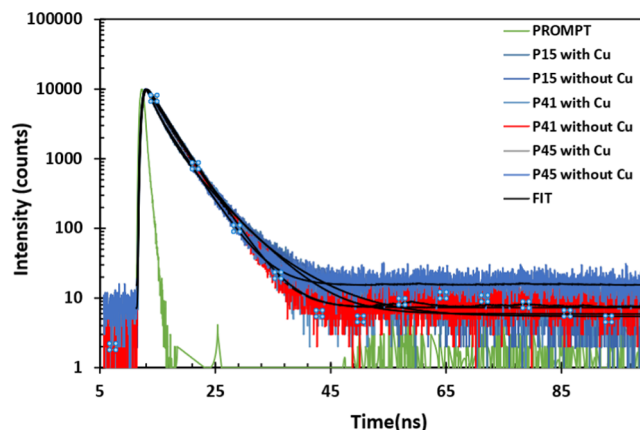
Figure 6. Fluorescence lifetime measurements of Rhodamine dyes and their metal complexes.

Table 1. Fluorescence Lifetime Measurements of Rhodamine Dyes and Their Metal Complexes

sample	T_1 (ns)	stdev	T_2 (ns)	std dev	χ^2
P15 without Cu	3.13	0.012	3.81	0.0012	1.4
P15 with Cu^{2+}	1.98	0.015	5.25	0.018	1.5
P41 without Cu	1.90	0.027	3.54	0.0092	1.3
P41 with Cu^{2+}	1.95	0.029	3.57	0.0089	1.2
P45 without Cu	0.78	0.0058	3.51	0.0058	1.1
P45 with Cu^{2+}	1.78	0.0027	3.51	0.0058	1.1

analyses were also conducted in addition to the Job's plots analyses. When the sensors were coordinated with Cu^{2+}, the amide N-H exhibited tautomerism to C=N, and the stretching vibration absorption peaks appeared at 1650 cm^{-1}
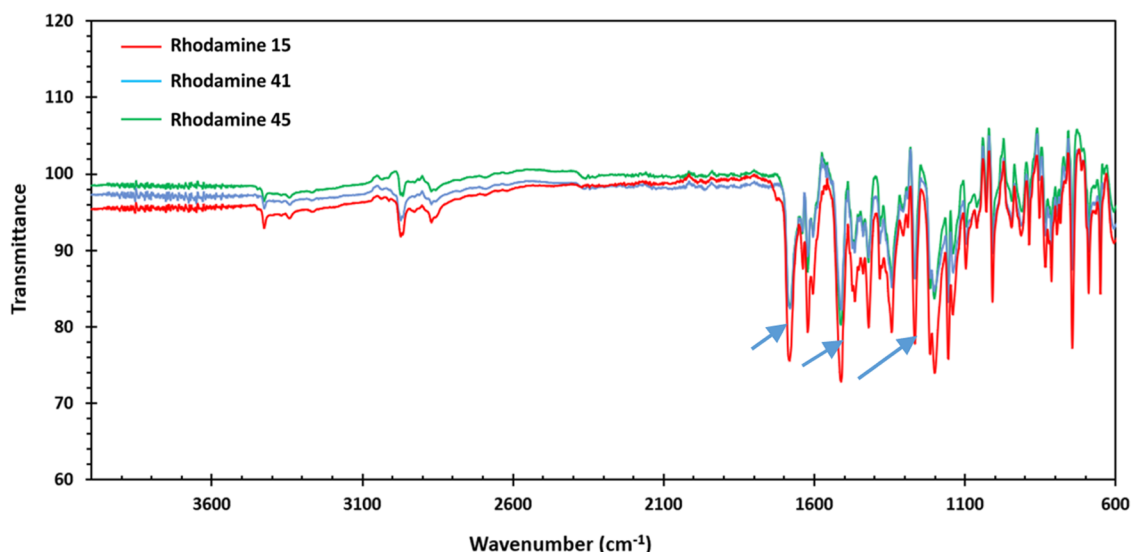
Figure 7. FT-IR spectrum of TiO$_2$ sensitized with rhodamine with and without copper.

in the IR spectra of the sensors. Once the spriolactam ring was opened due to Cu^{2+} binding, a new peak of C═N appeared at 1607 cm^{-1}, which was caused by the arylamine N-H tautomerism to C═N. The presence of nitrate confirms the peak at 1380 cm^{-1}. Therefore, IR data suggest that the sensors might complex with Cu^{2+} via the O−Cu^{2+}−O coordination bond as shown in Figure 7.

2.5. Current and Voltage Measurements. The solar to electric power efficiency of the rhodamine dye-sensitized solar cells was determined through current and voltage measurements of the fabricated device. The solar to electric power efficiency of the three rhodamine dyes was compared with the efficiencies of devices fabricated with rhodamine dye with copper. Figure 8 and Table 2 show the current density (I−V)
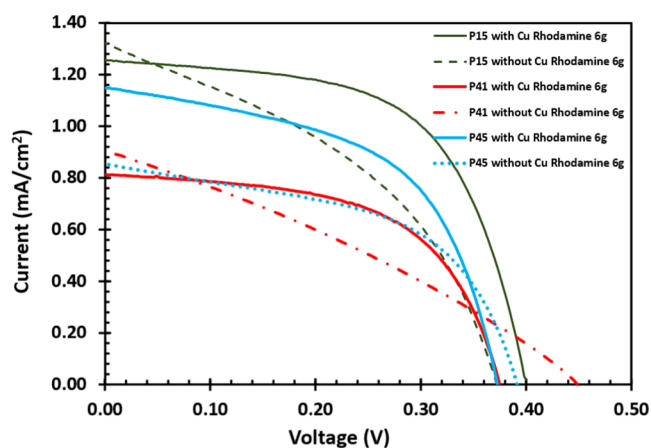

Figure 8. Current−voltage characteristics of the rhodamine dye-sensitized solar cell measured under air-mass 1.5 global (AM 1.5 G) illumination having an irradiance of 100 mW/cm^2.

characteristics of the samples under air-mass 1.5 global (AM 1.5 G) illumination having an irradiance of 100 mW/cm^2. In all three rhodamine dyes, an increase in efficiency was observed after the copper ion was made to react with the rhodamine dye. The efficiency of the device with **P45** was 0.18% but increased to 0.23% upon the addition of the copper (II) ion. Similarly, the solar to electric power efficiencies of

**Table 2. Current and Voltage Measurements for Rhodamine Dye-Sensitized Solar Cells**

	V_{max} (V)	I_{max} (mA/cm^2)	V_{oc} (V)	I_{sc} (mA/cm^2)	FF	efficiency (%)
P41 with Cu^{2+}	0.28	0.63	0.37	0.81	0.57	0.17
P41 without Cu	0.25	0.5	0.45	0.9	0.31	0.13
P45 with Cu^{2+}	0.28	0.83	0.37	1.15	0.54	0.23
P45 without Cu	0.29	0.61	0.39	0.85	0.53	0.18
P15 with Cu^{2+}	0.27	0.59	0.38	0.78	0.55	0.16
P15 without Cu	0.21	0.65	0.24	0.74	0.77	0.14

P41 and **P15** were 0.13 and 0.20%, respectively, but on introducing the copper (II) ion, the efficiencies jumped to 0.17 and 0.30% respectively. Thus, the introduction of copper enhanced the light absorption abilities of the rhodamine dye and consequently led to the increase in the efficiencies of the devices fabricated with them.

2.6. Impedance Measurements. Electrochemical impedance spectroscopy (EIS) was applied in the elucidation of the interfacial charge processes. Impedance measurements are used to explore the properties and quality of dye-sensitized solar cells.[43] They are normal tools utilized to study the kinetics and energetics of charge transport and recombination in fabricated dye-sensitized solar cells.[44] The impedance measurements of the rhodamine devices are displayed in the Nyquist plot in Figure 9 and Bode plot in Figure 10. The Nyquist plot displays the impedance data in semicircles in the low-frequency region of the spectra. In Figure 9, well-defined semicircles associated with the charge transfer resistance between the counter electrode and redox (I^-/I_3^-) electrolyte are displayed in the high-frequency regions. Small resistances are known to allow a faster electron transfer rate, which results in the improvement of the performance of the dye-sensitized solar cell. On the other hand, large resistance hinders the flow of electrons and reduces the efficiency of the dye-sensitized solar cell. In the
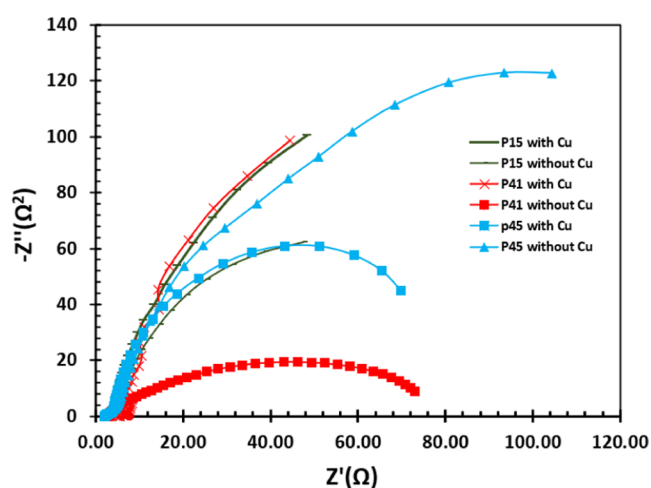
Figure 9. Nyquist plot of the rhodamine dye-sensitized solar cell measured under air-mass 1.5 global (AM 1.5 G) illumination having an irradiance of 100 mW/cm^2.
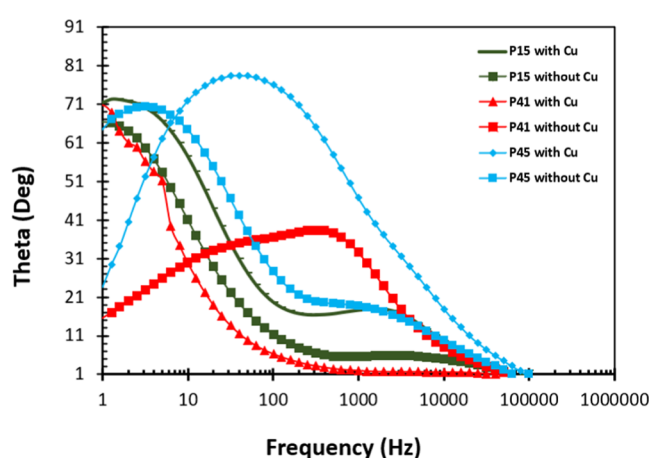
Figure 10. Bode plot of the rhodamine dye-sensitized solar cell measured under air-mass 1.5 global (AM 1.5 G) illumination having an irradiance of 100 mW/cm^2.

high-frequency region rhodamine **P45** with copper (II) ion shows the smallest charge transfer resistance compared to that of the other dyes. The results agree well with the current–voltage measurement that shows that **P45** with Cu^{2+} has the highest efficiency of 0.23%.

Using the Bode plots (Figure 10), the electron lifetimes (τ) of the DSSC devices created with rhodamine **P15**, **P41**, and **P45** with and without copper(II) ion were evaluated. Using the formula $\tau = 1/(2\pi f)$, where f is the frequency, the lifetimes of **P15**, **P41**, and **P45** with and without copper ion were calculated to be 83, 127, 125, 0.5, 4, and 50 ms. With rhodamine **P45** without copper, the lifetime 0.5 ms corresponded well with the V_{oc} in comparison with rhodamine **P45** with copper with a V_{oc} of 0.37 V but with a longer life lifetime of 50 ms and a corresponding high V_{oc} value of 0.39 V. The lifetime results and corresponding V_{oc} were not consistent with rhodamine 15 and 41 and their metal complexes, which could mean that factors other than the electron lifetime impacted the value of the open-circuit voltage. A longer τ means less electron recombination rate and an improvement in the V_{oc}.[45,46]

2.7. Analysis of the Simulation Outputs.

The oxygen vacancy from the TiO$_2$ lattice creates donor levels below 0.7–1.2 eV from the conduction band.[47] It resulted from the localization of electrons near V_O driven by the Madelung potential of the highly ionic crystal.[48,49] In the rutile phase of TiO$_2$, Ti interstitial defects are created more readily, while in the anatase phase, the oxygen vacancy is more favorable.[50] In the case of V_O, it was seen from DFT calculations within the generalized gradient approximation (GGA) that their positions are mostly in the subsurface level of TiO$_2$.[51] However, recent STM studies revealed that the subsurface-level V_O clusters get more stabilized in the surface level with the application of an external electric field.[52,53] The coupling between the 3d orbitals of the two undercoordinated Ti atoms at the surface V_O creates a σ bond and is predicted to be responsible for the stabilization of these deep-level defects.[39] According to DFT + U calculations, these defects are 1.5 eV below from the CBM and 2.2 eV above from the VBM.[35] We anticipate that oxygen vacancies at the surface level are produced in the TiO$_2$ lattice during the fabrication of our DSSC devices. To match with the experimental results, we have used deep-level V_O defects at the surface in our simulation study of the six DSSCs. The defects are positioned at the energy level of 2.2 eV above the VBM of TiO$_2$, and defect densities are modulated between 10^{14} and 10^{16} cm^{-3} to match with the experimental results. All the solar cell outputs from the experimental and computational analysis are shown in Supplementary Table S3 and Table 3.

Table 3. Efficiencies (Simulated and Experimental) for the Six DSSCs

| dye	simulated efficiency (%)	experimental efficiency (%)
P15 with Cu^{2+}	0.15	0.16
P15 without Cu	0.11	0.14
P41 with Cu^{2+}	0.16	0.17
P41 without Cu	0.12	0.13
P45 with Cu^{2+}	0.21	0.23
P45 without Cu	0.17	0.18

After using the parameters in Supplementary Table S1 in general for all devices and different absorbance data for each dye, our simulation results are matched with the experimental values utilizing the only possible defect configurations illustrated in Supplementary Table S2. Thus, we can anticipate that all the devices were subjected to deep-level oxygen vacancies at the surface having defect densities between 10^{14} and 10^{16} cm^{-3}. With increasing defect densities, conduction band electron recapture is accelerated, and it lowers the efficiency of the solar cells (Figure 11).

One of the key controlling parameters of the solar cells is the absorption factor, which influences the PV outputs mostly. Low recombination currents, larger open-circuit voltages, and higher conversion efficiencies all can be achieved with strong absorption of light by the absorber, especially in the long-wavelength area. A broad absorption band with an optimal overlap with the solar spectrum is one of the features that an ideal dye sensitizer should have.[50] Dyes with a high absorbance pick up more photons to excite electrons in the conduction band, creating more electron–hole pairs and convert photon energy to electrical energy. The overall efficiencies of our six devices are not significantly better compared to those of other DSSC devices, especially the devices made using N719 dye.[51–55] N719 has a broad absorption coefficient in the
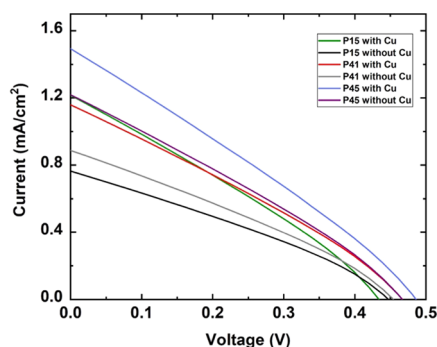
Figure 11. Current vs voltage graph of the six DSSCs from the simulation study.

region between 350 and 700 nm wavelength, and the solar spectrum AM 1.5 has the highest energy in this region also. For a clearer comparison, we plot all six dyes' absorbance with the N719 dye in Figure 12. Here, we can see that N719 dye has
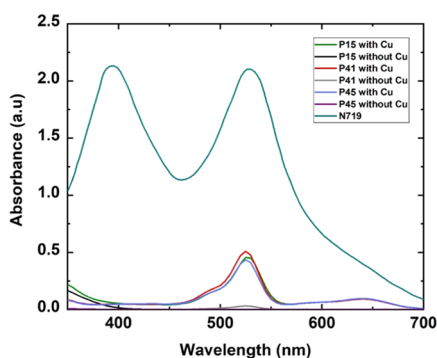
Figure 12. Comparison of absorption intensity of the six dyes with the N719 dye.

very high absorbance through the entire visible light region with two peaks at 395 and 530 nm. On the other hand, all the six dyes have very low absorbance in that region and have only one peak in the wavelength between 525 and 535 nm, which is also very low compared to that of N719 dye. The high absorbance of N719 dye-sensitized TiO_2 resulted in a photovoltaic efficiency of 6.45%,[51] whereas the weak absorbance intensity of our six dyes contributes to low device efficiency numbers in the current investigation.

3. CONCLUSIONS

In brief, we have developed a novel rhodamine 6G-based turn-on fluorescent sensor for Cu^{2+}. It displays high selectivity and sensitivity toward Cu^{2+} over other metal ions in aqueous media (pH = 7.2). Moreover, according to the study, **P41** and **P45** formed a 1:2 stoichiometry complex between sensors and Cu^{2+}, while **P15** formed a 1:1 complex with a Cu^{2+} complex. The compounds were further characterized using ^1H NMR, ^{13}C NMR, and HRMS. The solar to electric power efficiency of the metal complexes of the rhodamine dyes was higher than that of the devices fabricated with only rhodamine dyes. Surface-level oxygen vacancies (V_O) are the deep-level defects that are mostly present in TiO_2 nanostructures. Higher stability of V_O is achieved with an applied electric field. In SCAPS-1D software, we have used the parameters of Table S1 in general for all devices and to match with experimental results; individual absorbance data and the defect properties

demonstrated in Table S2 are used. Both simulated and experimental results for all the devices are almost identical, and the combination of high defects (Table S3) and low absorbance by the dyes (Figure 12) is responsible to generate these simulated results. From the simulation results, we can predict that it is indeed deep-level oxygen vacancies at the surface of TiO_2 of the order between 10^{14} and 10^{16} cm^{-3} that manifest in the DSSC devices. Furthermore, all six dyes also have very poor absorbance compared to that of the traditional N719 dye. These low absorbances also contributed to the low efficiencies of the devices.

4. EXPERIMENTAL SECTION

4.1. Materials and Methods. Rhodamine 6G, acetic acid, sodium hydroxide, hydrazine hydrate (85%), Isophthaldehyde, 2,5-furandicarboxaldehyde, 5-hydroxylmethyl-1,2-furaldehyde, and nitrate salts of Fe^{2+}, Fe^{3+}, Cu^{2+}, Cd^{2+}, Pb^{2+}, Zn^{2+}, Hg^{2+}, Ni^{2+}, Co^{2+}, Ca^{2+}, Mg^{2+}, Na^+, and K^+ used during the study were purchased from Sigma-Aldrich. The titanium dioxide film was prepared with Degussa P-25 powder acquired from the Institute of Chemical Education, Department of Chemistry, University of Wisconsin, Madison, WI. Colloidal graphite used in making the counter electrode was purchased from Ted Pella, Inc. The conducting fluorine-doped tin oxide (FTO) glass substrate was obtained from Hartford glass company, Hartford City, Indiana. Solvents including, ethanol, acetone, acetonitrile, and dimethyl sulfoxide were analytical grade and obtained from Sigma-Aldrich and used without further purification.

Microwave-assisted synthesis reactions were carried out in a CEM microwave reactor. The WS-650 Series spin processor used in spin-coating titanium dioxide on FTO glass was purchased from Laurell Technologies Corporation, PA. A UV−vis spectrophotometer was used to carry out absorption measurements using an Agilent Cary 60 UV−vis's spectrometer (Agilent, Walnut Creek, CA). Fluorescence spectra were measured using a Varian Cary Eclipse fluorescence spectrophotometer (Varian, Walnut Creek, CA). The slit width was 5 nm for both excitation and emission with 510 nm wavelength. Proton and carbon nuclear magnetic resonance (^1H and ^{13}C NMR) spectra were obtained using an Avance 400 MHz NMR spectrometer (Bruker Biospin, Billerica, MA). High-resolution mass spectrometry (HRMS) was recorded using a Bruker 12T solarix FT-ICR-MS. The IR spectrum was obtained using a Shimadzu IR Affinity-1S FTIR spectrometer (Shimadzu Scientific, Columbia, MD). The performance of the solar cell was evaluated using a 150 W fully reflective solar simulator with air-mass 1.5 global (AM 1.5 G) illumination, which comes with an irradiance of 100 mW/cm^2 (Sciencetech Inc.), London, Ontario, Canada, and the Reference 600 potentiostat/galvanostat/ZRA was purchased from GAMRY Instruments (Warminster, PA).

4.2. Synthesis of Rhodamine 6G Hydrazone (1). Rhodamine 6G hydrazone was synthesized according to Yang's method.[21] Rhodamine 6G (0.428 g, 1 mmol) was placed in a 50 mL flask. A total of 30 mL of ethanol was added. It was stirred continuously; 85% hydrazine was then added dropwise to the stirred solution. Then, the solution was heated to reflux for 12 h, and a pink precipitate appeared. The mixture was removed via filtration, washed with cold water:ethanol (1:1, v/v), and dried under vacuum. The reaction yielded 78 g of pure 1. ^1H NMR (DMSO-d_6), δ (ppm): 1.21 (t, 6H, NCH_2CH_3, J = 11.4 Hz), 1.87 (s, 6H, $-CH_3$), 3.14 (t, 4H, NCH_2CH_3, J = 12.0 Hz), 4.23 (s, $-NH_2$), 5.01(s, NH), 6.10

(s, 2H) 6.27 (s, 2H), 6.95 (d, 1H, J = 3.4 Hz), 7.47 (d, 1H, J = 2.9), 7.47(d, 1H, J = 3.3), 7.85(t, 1H, J = 2.6). Anal calcd for Rhodamine 6G hydrozone ($C_{26}H_{28}N_4O_2$): H 6.59, C 72.86, N 13.08; found: H 6.21, C 73.02, N 12.92.

4.3. Synthesis of R15. A mixture of 1 (100 mg, 0.219 mmol), phthalaldehyde (16 mg, 0.219 mmol), and ethanol (2 mL) was placed in a 10 mL reaction vial. The resulting mixture was stirred to make it homogeneous and placed in the cavity of a CEM microwave reactor. The closed reaction vessel was run under pressure and irradiated. The resulting solid was filtered and washed three times with cold ethanol. After drying, the product **R15** was isolated and obtained in 80% yield. ^{1}H NMR (DMSO), δ (ppm): 9.37 (2H, s, N=C-H); 7.94 (2H, d), 7.58 (4H, m), 7.34 (2H, m, H-Ar), 7.26 (2H, m, H-Ar), 7.05 (2H, d, H-Ar), 6.31 (4H, s), 6.19 (4H, s), 4.96 (4H, t), 3.08 (8H, q, NCH$_2$CH$_3$), 1.85 (12H, s, −CH3), 1.17 (12H, t, NCH$_2$CH$_3$). ^{13}C NMR (DMSO-d_6), δ (ppm): 163.70, 151.24, 151.06, 147.60, 145.59, 133.82, 132.98, 134.95, 129.92, 128.84, 128.72, 126.82, 125.92, 123.82, 123.09, 118.09, 105.24, 99.50, 95.80, 65.89, 37.42, 16.98, 14.21, 14.11. HRMS (MALDI): m/z calcd for **P15**: 955.4653; found: 955.4691.

4.4. Synthesis of R41. A mixture of 1 (100 mg, 0.219 mmol), 2,5-furandicarboxaldeyde (16 mg, 0.219 mmol), and ethanol (2 mL) was placed in a 10 mL reaction vial. The resulting mixture was stirred to make it homogeneous and placed in the cavity of a CEM microwave reactor. The closed reaction vessel was run under pressure and irradiated. The resulting solid was filtered and washed three times with cold ethanol. After drying, the product **R41** was isolated and obtained in 80% yield. ^{1}H NMR (DMSO-d_6), δ (ppm): 8.07 (2H, s, N=CH); 7.87 (2H, d), 7.54 (4H, m), 6.95 (2H, d), 6.66 (2H, s), 6.33 (4H, s), 6.17 (4H, s), 5.02 (4H, s), 3.15 (8H, q, NCH$_2$CH$_3$), 1.82 (12H, s, −CH$_3$), 1.21 (12H, t, NCH$_2$CH$_3$). ^{13}C NMR (DMSO-d_6), δ (ppm): 164.01, 152.31, 150.60, 150.41, 147.91, 134.12, 134.04, 128.48, 128.57, 127.10, 126.36, 123.38, 123.06, 118.49, 115.07, 104.22, 96.03, 65.07, 37.48, 16.85, 14.18. HRMS (MALDI): m/z calcd for **P41**: 945.4446; found: 945.4485.

4.5. Synthesis of R45. A mixture of 1 (100 mg, 0.219 mmol), 5-hydroxymethyl-2-furaldehyde (16 mg, 0.219 mmol), and ethanol (2 mL) was placed in a 10 mL reaction vial. The resulting mixture was stirred to make it homogeneous and placed in the cavity of a CEM microwave reactor. The closed reaction vessel was run under pressure and irradiated. The resulting solid was filtered and washed three times with cold ethanol. After drying, the product **R45** was isolated and obtained in 85% yield. 1H NMR (DMSO), δ (ppm): 7.76 (1H, s, N=C-H); 7.48 (2H, t), 6.64 (1H, d), 6.26 (2H, s), 6.09 (2H, s), 5.2 (2H, t), 4.23 (2H, s), 3.34 (2H, s), 3.31 (4H, q, NCH$_2$CH$_3$), 1.90 (6H, s, −CH$_3$), 1.14 (6H, t, NCH$_2$CH$_3$). 13C NMR (DMSO), δ (ppm): 165.23, 152.07, 151.33, 147.35, 132.31, 129.48, 128.00, 127.01, 123.43, 122.13, 117.79, 104.99, 95.85, 64.96, 55.99, 37.45, 18.53, 17.06, 14.20. HRMS (MALDI): m/z calcd for **P45**: 537.2496; found: 537.2499.

4.6. Preparation of Titanium Dioxide. The titanium dioxide paste was prepared by mixing titanium dioxide powder and glacial acetic acid. The titanium dioxide paste was subsequently spin-coated on FTO glass and annealed at 450 °C for 30 min.

4.7. Fabrication of the DSSC. The components of the solar cell were assembled by placing the dye-sensitized titanium dioxide on top of the graphite-coated FTO glass followed by the introduction of the electrolyte between them.

First, the annealed TiO$_2$ was first immersed in the rhodamine and left overnight. The cathode was prepared by applying colloidal graphite on the conductive surface of the FTO glass.

4.8. Simulation Methods. SCAPS-1D version 3.3.03 simulation software was developed by the Department of Electronics and Information Systems (ELIS) of the University of Gent in Belgium. Almost all parameters of a solar cell (E_g, χ, ε, N_C, N_V, v_{thn}, v_{thp}, μ_n, μ_p, N_a, N_d, N_t) can be graded in SCAPS-1D. A maximum of seven stacked solar cell architectures can be simulated through the software tool. The simulation results are used to analyze the impact on device performance and get crucial insights into fundamental solar properties such as material defect density, location and level, recombination, and bandgap alignment between device layers. These physical quantities can be computed at different illumination and temperature levels and under both light and dark conditions. The primary function of SCAPS is to solve one-dimensional semiconductor equations. In the bulk of the layers, these equations are Poisson's and continuity equations for holes and electrons. The continuity equation is as follows

$$\frac{dp}{dt} = -\frac{1}{q} \nabla J_p - R(x) + G(x) \tag{1}$$

$$\frac{dn}{dt} = -\frac{1}{q} \nabla J_n - R(x) + G(x) \tag{2}$$

J_n and J_p are the electron and hole current densities, respectively, and $R(x)$ and $G(x)$ are the recombination and generation rates, respectively. Drift-diffusion equations for electrons and holes are as follows,

$$J_n = qn(x)\mu_n \frac{dv(x)}{dx} + qD_n \frac{dn(x)}{dx} \tag{3}$$

$$J_p = qn(x)\mu_p \frac{dv(x)}{dx} + qD_p \frac{dn(x)}{dx} \tag{4}$$

where μ_n and μ_p represent the mobility of electrons and holes, respectively, and D_n and D_p represent the diffusion constants for electrons and holes, respectively. The generation rates mentioned in drift-diffusion equations are as follows

$$G(\lambda, x) = \alpha(\lambda)N_{photo}(\lambda, x) \tag{5}$$

$$G(x) = \int_{\lambda_{min}}^{\lambda_{max}} G(\lambda, x)d\lambda \tag{6}$$

where $N_{photo}(\lambda, x)$ represents the photon flux at point x, $N_{photo0}(\lambda)$ represents the photon flux at position $x = 0$, and $\alpha(\lambda)$ represents the absorption coefficient. G stands for generation rates. The Poisson equation is as follows

$$\nabla^2 V(x) = \frac{q}{\in}[p(x) - n(x) + N_d^+ - N_a^-] \tag{7}$$

where, $V(x)$ is the electrostatic potential, ϵ is the absorber permittivity, q is the electron charge, N_a and N_d are acceptor and donor dopant densities, respectively, and $p(x)$ and $n(x)$ are position-dependent electron and hole concentrations, respectively. SCAPS solves the abovementioned equations for one-dimensional semiconductor in the bulk of the layers given by

$$J_n = -\frac{\mu_n n}{q} \frac{dE_{F_n}}{dx} \tag{8}$$

$$\frac{\mathrm{d}p_n}{\mathrm{d}t} = G_p - \frac{p_n - p_{n_0}}{\tau_p} - p_n \mu_p \frac{\mathrm{d}\xi}{\mathrm{d}x} - \mu_p \xi \frac{\mathrm{d}p_n}{\mathrm{d}x} + D_p \frac{\mathrm{d}^2 p_n}{\mathrm{d}x^2} \quad (9)$$

$$\frac{\mathrm{d}n_p}{\mathrm{d}t} = G_n - \frac{n_p - n_{p_0}}{\tau_n} + n_p \mu_n \frac{\mathrm{d}\xi}{\mathrm{d}x} + \mu_n \xi \frac{\mathrm{d}n_p}{\mathrm{d}x} + D_n \frac{\mathrm{d}^2 n_p}{\mathrm{d}x^2} \quad (10)$$

Using proper boundary conditions, the abovementioned equations are solved to get the photovoltaic outputs of the DSSC devices.

The device fill factor (FF) and efficiency (η) are measured using the following equations

$$\mathrm{FF} = \frac{V_{\mathrm{MP}} \cdot J_{\mathrm{MP}}}{V_{\mathrm{OC}} \cdot J_{\mathrm{SC}}} \quad (11)$$

$$\eta = \frac{V_{\mathrm{OC}} \cdot J_{\mathrm{SC}} \cdot \mathrm{FF}}{P_{\mathrm{in}}} \quad (12)$$

where P_{in} is the input power and J_{MP} and V_{MP} are the current density and voltage at the maximum power point, respectively.

ASSOCIATED CONTENT

Supporting Information

The Supporting Information is available free of charge at https://pubs.acs.org/doi/10.1021/acsomega.1c06772.

Additional data, ^{1}H NMR, ^{13}C NMR, HRMS, and simulation parameter tables (PDF)

AUTHOR INFORMATION

Corresponding Authors

Jamal Uddin − Center for Nanotechnology, Department of Natural Sciences, Coppin State University, Baltimore, Maryland 21216, United States; orcid.org/0000-0002-6714-9286; Email: juddin@coppin.edu

Fasil Abebe − Department of Chemistry, Morgan State University, Baltimore, Maryland 21251, United States; orcid.org/0000-0002-4859-7059; Email: Fasil.Abebe@morgan.edu

Authors

Oyedoyin Aduroja − Department of Chemistry, Morgan State University, Baltimore, Maryland 21251, United States

MdRafsun Jani − Department of Materials and Metallurgical Engineering (MME), Bangladesh University of Engineering and Technology (BUET), Dhaka 1000, Bangladesh

William Ghann − Center for Nanotechnology, Department of Natural Sciences, Coppin State University, Baltimore, Maryland 21216, United States

Saquib Ahmed − Department of Mechanical Engineering Technology, SUNY − Buffalo State, Buffalo, New York 14222, United States; orcid.org/0000-0001-6251-6297

Complete contact information is available at:
https://pubs.acs.org/10.1021/acsomega.1c06772

Notes

The authors declare no competing financial interest.

ACKNOWLEDGMENTS

REFERENCES

(1) O'Regan, B.; Grätzel, M. A Low-Cost, High-Efficiency Solar Cell Based on Dye-Sensitized Colloidal TiO2 Films. Nature 1991, 353, 737−740.

(2) Ghann, W.; Kang, H.; Sheikh, T.; Yadav, S.; Chavez-Gil, T.; Nesbitt, F.; Uddin, J. Fabrication, Optimization and Characterization of Natural Dye Sensitized Solar Cell. Sci. Rep. 2017, 7, No. 41470.

(3) Ghann, W.; Sobhi, H.; Kang, H.; Chavez-Gil, T.; Nesbitt, F.; Uddin, J. Synthesis and Characterization of Free and Copper (II) Complex of N,N′-Bis(Salicylidene)Ethylenediamine for Application in Dye Sensitized Solar Cells. J. Mater. Sci. Chem. Eng. 2017, 05, 46−66.

(4) Chang, W.-C.; Chen, H.-S.; Li, T.-Y.; Hsu, N.-M.; Tingare, Y. S.; Li, C.-Y.; Liu, Y.-C.; Su, C.; Li, W.-R. Highly Efficient N-Heterocyclic Carbene/Pyridine-Based Ruthenium Sensitizers: Complexes for Dye-Sensitized Solar Cells. Angew. Chem., Int. Ed. 2010, 49, 8161−8164.

(5) Chen, H.-S.; Chang, W.-C.; Su, C.; Li, T.-Y.; Hsu, N.-M.; Tingare, Y. S.; Li, C.-Y.; Shie, J.-H.; Li, W.-R. Carbene-Based Ruthenium Photosensitizers. Dalton Trans. 2011, 40, 6765−6770.

(6) Dai, F.; Wu, W.; Wang, Q.; Tian, H.; Wong, W. Heteroleptic Ruthenium Complexes Containing Uncommon 5,5′-Disubstituted-2,2′-Bipyridine Chromophores for Dye-Sensitized Solar Cells. Dalton Trans. 2011, 40, 2314−2323.

(7) Islam, A.; Singh, S. P.; Yanagida, M.; Karim, M. R.; Han, L. Amphiphilic Ruthenium(II) Terpyridine Sensitizers with Long Alkyl Chain Substituted β-Diketonato Ligands: An Efficient Coadsorbent-Free Dye-Sensitized Solar Cells. Int. J. Photoenergy 2011, 2011, No. e757421.

(8) Kuang, D.; Klein, C.; Ito, S.; Moser, J.-E.; Humphry-Baker, R.; Evans, N.; Duriaux, F.; Grätzel, C.; Zakeeruddin, S. M.; Grätzel, M. High-Efficiency and Stable Mesoscopic Dye-Sensitized Solar Cells Based on a High Molar Extinction Coefficient Ruthenium Sensitizer and Nonvolatile Electrolyte. Adv. Mater. 2007, 19, 1133−1137.

(9) Chen, C.-Y.; Wu, S.-J.; Li, J.-Y.; Wu, C.-G.; Chen, J.-G.; Ho, K.-C. A New Route to Enhance the Light-Harvesting Capability of Ruthenium Complexes for Dye-Sensitized Solar Cells. Adv. Mater. 2007, 19, 3888−3891.

(10) Oh, J.; Ghann, W.; Kang, H.; Nesbitt, F.; Providence, S.; Uddin, J. Comparison of the Performance of Dye Sensitized Solar Cells Fabricated with Ruthenium Based Dye Sensitizers: Di-Tetrabutylammonium Cis-Bis(Isothiocyanato)Bis(2,2′-Bipyridyl-4,4′-Dicarboxylato)Ruthenium(II) (N719) and Tris(Bipyridine)-Ruthenium(II) Chloride (Ru-BPY). Inorg. Chim. Acta 2018, 482, 943−950.

(11) Birel, Ö.; Nadeem, S.; Duman, H. Porphyrin-Based Dye-Sensitized Solar Cells (DSSCs): A Review. J. Fluoresc. 2017, 27, 1075−1085.

(12) Yella, A.; Lee, H.-W.; Tsao, H. N.; Yi, C.; Chandiran, A. K.; Nazeeruddin, MdK.; Diau, E. W.-G.; Yeh, C.-Y.; Zakeeruddin, S. M.; Grätzel, M. Porphyrin-Sensitized Solar Cells with Cobalt (II/III)−Based Redox Electrolyte Exceed 12 Percent Efficiency. Science 2011, 334, 629−634.

(13) Lu, J.; Liu, S.; Wang, M. Push-Pull Zinc Porphyrins as Light-Harvesters for Efficient Dye-Sensitized Solar Cells. Front. Chem. 2018, 6, No. 541.

(14) Ghann, W.; Chavez-Gil, T.; Goede, C. I.; Kang, H.; Khan, S.; Sobhi, H.; Nesbitt, F.; Uddin, J. Photophysical, Electrochemical and Photovoltaic Properties of Porphyrin-Based Dye Sensitized Solar Cell. Adv. Mater. Phys. Chem. 2017, 07, 148−172.

(15) Ghann, W.; Kang, H.; Emerson, E.; Oh, J.; Chavez-Gil, T.; Nesbitt, F.; Williams, R.; Uddin, J. Photophysical Properties of Near-IR Cyanine Dyes and Their Application as Photosensitizers in Dye Sensitized Solar Cells. *Inorg. Chim. Acta* **2017**, *467*, 123−131.

(16) Wu, W.; Guo, F.; Li, J.; He, J.; Hua, J. New Fluoranthene-Based Cyanine Dye for Dye-Sensitized Solar Cells. *Synth. Met.* **2010**, *160*, 1008−1014.

(17) Pepe, G.; Cole, J. M.; Waddell, P. G.; McKechnie, S. Molecular Engineering of Cyanine Dyes to Design a Panchromatic Response in Co-Sensitized Dye-Sensitized Solar Cells. *Mol. Syst. Des. Eng.* **2016**, *1*, 86−98.

(18) Hug, H.; Bader, M.; Mair, P.; Glatzel, T. Biophotovoltaics: Natural Pigments in Dye-Sensitized Solar Cells. *Appl. Energy* **2014**, *115*, 216−225.

(19) Das, S. K.; Ganguli, S.; Kabir, H.; Khandaker, J. I.; Ahmed, F. Performance of Natural Dyes in Dye-Sensitized Solar Cell as Photosensitizer. *Trans. Electr. Electron. Mater.* **2020**, *21*, 105−116.

(20) Richhariya, G.; Kumar, A.; Tekasakul, P.; Gupta, B. Natural Dyes for Dye Sensitized Solar Cell: A Review. *Renewable Sustainable Energy Rev.* **2017**, *69*, 705−718.

(21) Maiaugree, W.; Lowpa, S.; Towannang, M.; Rutphonsan, P.; Tangtrakarn, A.; Pimanpang, S.; Maiaugree, P.; Ratchapolthavisin, N.; Sang-aroon, W.; Jarernboon, W.; Amornkitbamrung, V. A Dye Sensitized Solar Cell Using Natural Counter Electrode and Natural Dye Derived from Mangosteen Peel Waste. *Sci. Rep.* **2015**, *5*, No. 15230.

(22) Iwuji, C.; Ghann, W.; Iwuji, O.; Uddin, J. *Rhodamine 800 as a Sensitizer for Dye Sensitized Solar Cells* 2018, 4.

(23) Jones, A. P.; Ghann, W.; Uddin, J. Indocyanine Green as a Sensitizer for Dye-Sensitized Solar Cell https://www.semanticscholar.org/paper/Indocyanine-Green-as-a-Sensitizer-for-Solar-Cell-Jones-Ghann/df5560f8cbc198fecfa9d6410cc015b55487a4cd (accessed Nov 15, 2021).

(24) Calogero, G.; Sinopoli, A.; Citro, I.; Marco, G. D.; Petrov, V.; Diniz, A. M.; Parola, A. J.; Pina, F. Synthetic Analogues of Anthocyanins as Sensitizers for Dye-Sensitized Solar Cells. *Photochem. Photobiol. Sci.* **2013**, *12*, 883−894.

(25) Moniruddin, M.; Ilyassov, B.; Seliverstova, E.; Shabdan, Y.; Bakranov, N.; Ibrayev, N.; Nuraje, N. Bioinspired Study of Energy and Electron Transfer in Photovoltaic System. *J. Exp. Nanosci.* **2017**, *12*, 285−296.

(26) Beija, M.; Afonso, C. A. M.; Martinho, J. M. G. Synthesis and Applications of Rhodamine Derivatives as Fluorescent Probes. *Chem. Soc. Rev.* **2009**, *38*, 2410−2433.

(27) Abebe, F.; Perkins, P.; Shaw, R.; Tadesse, S. A Rhodamine-Based Fluorescent Sensor for Selective Detection of Cu2+ in Aqueous Media: Synthesis and Spectroscopic Properties. *J. Mol. Struct.* **2020**, *1205*, No. 127594.

(28) Pan, X.; Yang, M.-Q.; Fu, X.; Zhang, N.; Xu, Y.-J. Defective TiO2 with Oxygen Vacancies: Synthesis, Properties and Photo-catalytic Applications. *Nanoscale* **2013**, *5*, 3601−3614.

(29) Nakamura, I.; Negishi, N.; Kutsuna, S.; Ihara, T.; Sugihara, S.; Takeuchi, K. Role of Oxygen Vacancy in the Plasma-Treated TiO2 Photocatalyst with Visible Light Activity for NO Removal. *J. Mol. Catal. A: Chem.* **2000**, *161*, 205−212.

(30) Pacchioni, G. Oxygen Vacancy: The Invisible Agent on Oxide Surfaces. *ChemPhysChem* **2003**, *4*, 1041−1047.

(31) Ako, R. T.; Ekanayake, P.; Young, D. J.; Hobley, J.; Chellappan, V.; Tan, A. L.; Gorelik, S.; Subramanian, G. S.; Lim, C. M. Evaluation of Surface Energy State Distribution and Bulk Defect Concentration in DSSC Photoanodes Based on Sn, Fe, and Cu Doped TiO2. *Appl. Surf. Sci.* **2015**, *351*, 950−961.

(32) Thomas, A. G.; Flavell, W. R.; Mallick, A. K.; Kumarasinghe, A. R.; Tsoutsou, D.; Khan, N.; Chatwin, C.; Rayner, S.; Smith, G. C.; Stockbauer, R. L.; Warren, S.; Johal, T. K.; Patel, S.; Holland, D.; Taleb, A.; Wiame, F. Comparison of the Electronic Structure of Anatase and Rutile ${\mathrm{TiO}}_{2}$ Single-Crystal Surfaces Using Resonant Photoemission and x-Ray Absorption Spectroscopy. *Phys. Rev. B* **2007**, *75*, No. 035105.

(33) Setvin, M.; Hao, X.; Daniel, B.; Pavelec, J.; Novotny, Z.; Parkinson, G. S.; Schmid, M.; Kresse, G.; Franchini, C.; Diebold, U. Charge Trapping at the Step Edges of TiO2 Anatase (101). *Angew. Chem., Int. Ed.* **2014**, *53*, 4714−4716.

(34) Setvin, M.; Franchini, C.; Hao, X.; Schmid, M.; Janotti, A.; Kaltak, M.; Van de Walle, C. G.; Kresse, G.; Diebold, U. Direct View at Excess Electrons in ${\mathrm{TiO}}_{2}$ Rutile and Anatase. *Phys. Rev. Lett.* **2014**, *113*, No. 086402.

(35) Wang, X.; Feng, Z.; Shi, J.; Jia, G.; Shen, S.; Zhou, J.; Li, C. Trap States and Carrier Dynamics of TiO2 Studied by Photo-luminescence Spectroscopy under Weak Excitation Condition. *Phys. Chem. Chem. Phys.* **2010**, *12*, 7083−7090.

(36) Cheng, H.; Selloni, A. Surface and Subsurface Oxygen Vacancies in Anatase ${\text{TiO}}_{2}$ and Differences with Rutile. *Phys. Rev. B* **2009**, *79*, No. 092101.

(37) Setvin, M.; Schmid, M.; Diebold, U. Aggregation and Electronically Induced Migration of Oxygen Vacancies in ${\mathrm{TiO}}_{2}$ Anatase. *Phys. Rev. B* **2015**, *91*, No. 195403.

(38) Naldoni, A.; Allieta, M.; Santangelo, S.; Marelli, M.; Fabbri, F.; Cappelli, S.; Bianchi, C. L.; Psaro, R.; Dal Santo, V. Effect of Nature and Location of Defects on Bandgap Narrowing in Black TiO2 Nanoparticles. *J. Am. Chem. Soc.* **2012**, *134*, 7600−7603.

(39) Hao, Y.-n.; Chen, T.; Zhang, X.; Zhou, H.; Ma, Y. Ti-Ti σ Bond at Oxygen Vacancy Inducing the Deep Defect Level in Anatase TiO2 (101) Surface. *J. Chem. Phys.* **2019**, *150*, No. 224702.

(40) Nowotny, M. K.; Bak, T.; Nowotny, J. Electrical Properties and Defect Chemistry of TiO2 Single Crystal. I. Electrical Conductivity. *J. Phys. Chem. B* **2006**, *110*, 16270−16282.

(41) Lu, G.; Linsebigler, A.; Yates, J. T. Ti3+ Defect Sites on TiO2(110): Production and Chemical Detection of Active Sites. *J. Phys. Chem. A* **1994**, *98*, 11733−11738.

(42) Thompson, T. L.; Yates, J. T. TiO2-Based Photocatalysis: Surface Defects, Oxygen and Charge Transfer. *Top. Catal.* **2005**, *35*, 197−210.

(43) Porto, S. P. S.; Fleury, P. A.; Damen, T. C. Raman Spectra of TiO2, MgF2, ZnF2, FeF2, and MnF2. *Phys. Rev.* **1967**, *154*, 522−526.

(44) Pan, X.; Yang, M. Q.; Fu, X.; Zhang, N.; Xu, Y. J. Defective TiO2 with Oxygen Vacancies: Synthesis, Properties and Photo-catalytic Applications. *Nanoscale* **2013**, *5*, 3601−3614.

(45) Pacchioni, G. Oxygen Vacancy: The Invisible Agent on Oxide Surfaces. *ChemPhysChem* **2003**, *4*, 1041−1047.

(46) Morgan, B. J.; Watson, G. W. Erratum: Intrinsic n-Type Defect Formation in TiO 2: A Comparison of Rutile and Anatase from GGA + U Calculations (Journal of Physical Chemistry C (2010) 114:5 (2321-2328) DOI: 10.1021/Jp9088047). *J. Phys. Chem. C* **2012**, *116*, 7242.

(47) Cheng, H.; Selloni, A. Surface and Subsurface Oxygen Vacancies in Anatase TiO2 and Differences with Rutile. *Phys. Rev. B: Condens. Matter Mater. Phys.* **2009**, *79*, 2−5.

(48) Setvin, M.; Schmid, M.; Diebold, U. Aggregation and Electronically Induced Migration of Oxygen Vacancies in TiO2 Anatase. *Phys. Rev. B: Condens. Matter Mater. Phys.* **2015**, *91*, 1−9.

(49) Cheng, H.; Selloni, A. Energetics and Diffusion of Intrinsic Surface and Subsurface Defects on Anatase TiO2 (101). *J. Chem. Phys.* **2009**, *131*, No. 054703.

(50) Clifford, J. N.; Martínez-Ferrero, E.; Viterisi, A.; Palomares, E. Sensitizer Molecular Structure-Device Efficiency Relationship in Dye Sensitized Solar Cells. *Chem. Soc. Rev.* **2011**, *40*, 1635−1646.

(51) Prima, E. C.; Nugroho, H. S.; Refantero, G.; Panatarani, C.; Yuliarto, B.; Nugraha. Performance of the Dye-Sensitized Quasi-Solid State Solar Cell with Combined Anthocyanin-Ruthenium Photo-sensitizer. *RSC Adv.* **2020**, *10*, 36873−36886.

(52) Paquin, F.; Rivnay, J.; Salleo, A.; Stingelin, N.; Silva, C. Multi-Phase Semicrystalline Microstructures Drive Exciton Dissociation in Neat Plastic Semiconductors. *J. Mater. Chem. C* **2015**, *3*, 10715−10722.

(53) Tao, L.; Huo, Z.; Ding, Y.; Li, Y.; Dai, S.; Wang, L.; Zhu, J.; Pan, X.; Zhang, B.; Yao, J.; Nazeeruddin, M. K.; Grätzel, M. High-Efficiency and Stable Quasi-Solid-State Dye-Sensitized Solar Cell

Based on Low Molecular Mass Organogelator Electrolyte. *J. Mater. Chem. A* **2015**, *3*, 2344–2352.

(54) Manuscript, A.; Society, R.; Manuscripts, A.; Manuscript, T. A.; Manuscripts, A.; Society, R.; Manuscript, A. RSC Advances.

(55) Wang, X.; Bolag, A.; Yun, W.; Du, Y.; Eerdun, C.; Zhang, X.; Bao, T.; Ning, J.; Alata, H.; Ojiyed, T. Enhanced Performance of Dye-Sensitized Solar Cells Based on a Dual Anchored Diphenylpyranylidene Dye and N719 Co-Sensitization. *J. Mol. Struct.* **2020**, *1206*, No. 127694.